Chaos, Solitons and Fractals 202 (2026) 117479

Contents lists available at ScienceDirect

Chaos, Solitons and Fractals

journal homepage: www.elsevier.com/locate/chaos

Studying synchronization of neural oscillators through NMDA-AMPA receptor interactions

Hamid Mofidi [a,b,*], Yangyang Wang [c]

[a] Beijing Institute of Mathematical Sciences and Applications (BIMSA), Beijing 101408, China
[b] Yau Mathematical Sciences Center (YMSC), Tsinghua University, Beijing 100084, China
[c] Department of Mathematics, Brandeis University, Waltham, MA 02453, United States of America

ARTICLE INFO

Keywords:
Neural synchronization
NMDA receptors
AMPA receptors
Morris-Lecar model
Bifurcation analysis
Phase-locking value

ABSTRACT

This study investigates how NMDA and AMPA receptors influence synchronization in neural oscillators modeled by coupled Morris–Lecar systems. By analyzing the interplay between receptor kinetics, synaptic coupling strengths, and voltage-dependent magnesium block, we identify the mechanisms that govern neural synchronization. We show that fast AMPAR kinetics yield perfect synchrony at substantially lower coupling than NMDARs, which produce only near-synchrony even when Mg^{2+} block is absent. To resolve subtle regimes, we pair a time-domain mean phase difference (MPD) with the phase-locking value (PLV) and overlay bifurcation continuations (LP/HB/PD), exposing boundaries that PLV alone can miss. Although NMDARs sustain prolonged conductance, their slow decay and Mg^{2+} dependence blur spike timing and limit precise locking. These results provide a quantitative, mechanism-based account of glutamatergic control of synchrony and suggest experimentally testable predictions relevant to coordination deficits in disorders such as schizophrenia.

1. Introduction

Neural synchronization is a fundamental mechanism underlying brain function, enabling processes ranging from motor control to cognitive functions such as attention, perception, and memory [1,2]. At the core of these dynamics lies synaptic transmission, where neurotransmitters mediate communication between neurons via ionotropic receptors. Among these, glutamatergic α-amino-3-hydroxy-5-methyl-4-isoxazolepropionic acid (AMPA) and N-methyl-D-aspartate (NMDA) receptors play distinct yet complementary roles in shaping network rhythms [3,4]. AMPA receptors (AMPARs) are known for their fast kinetics and voltage-independent activation, making them ideal for rapid signal transmission. In contrast, NMDA receptors (NMDARs) exhibit slower kinetics, and voltage-dependent magnesium block [5]. While both receptors are critical for neural communication, their distinct yet complementary contributions to network synchronization, particularly how their timescales and magnesium block interact, remain unresolved. However, whether NMDA receptor-mediated currents alone can produce stable, perfect synchronization remains unclear.

Computational studies of neural networks, particularly those modeling central pattern generators and respiratory rhythms, have traditionally focused on AMPAR-mediated mechanisms [6–8]. For example, models of preBötzinger complex neurons have successfully replicated respiratory rhythms using AMPAR-like coupling, often omitting NMDAR dynamics [9]. This aligns with experimental evidence showing that AMPAR antagonists abolish respiratory rhythms [10,11]. However, emerging studies suggest that NMDARs can sustain rhythms under specific conditions, such as in magnesium-free solutions or during developmental stages [12,13]. Despite these findings, few computational studies have systematically compared the roles of AMPARs and NMDARs

* Corresponding author at: Beijing Institute of Mathematical Sciences and Applications (BIMSA), Beijing 101408, China.
E-mail addresses: h.mofidi@bimsa.cn (H. Mofidi), yangyangwang@brandeis.edu (Y. Wang).

https://doi.org/10.1016/j.chaos.2025.117479
Received 13 August 2025; Received in revised form 5 October 2025; Accepted 24 October 2025
Available online 3 November 2025

in synchronization dynamics. Notable exceptions include Castellani et al. [14], who modeled bidirectional synaptic plasticity but did not address network-level synchronization, and Gauck & Jaeger [15], who analyzed cerebellar nuclei spiking without bifurcation analysis. This leaves a critical gap in understanding how receptor-specific timescales and magnesium block interact to regulate phase-locking in neural networks.

Early theoretical and numerical studies had already pointed out that purely slow, NMDA-like coupling tends to desynchronize or produce only loosely coordinated activity, whereas fast AMPA-mediated synapses favor robust in-phase locking in two-cell and network models [12,16–20]. The present work builds on those principles by quantifying the exact parameter ranges over which each receptor type controls phase locking in biophysically detailed Morris–Lecar oscillators.

In this study, we investigate the roles of AMPARs and NMDARs in synchronization using bidirectionally coupled Morris–Lecar (ML) oscillators. Within this framework, calcium currents are represented through their steady-state activation $m_\infty(V_i)$ rather than dynamic gating, which does not incorporate the calcium permeability of NMDARs. Despite this simplification, the model retains essential biophysical features and allows direct examination of how NMDARs' voltage-dependent magnesium block ($B(V_i)$) and their characteristically slow decay kinetics fundamentally limit their synchronization efficacy compared to AMPARs. Key aspects of this work include:

(i) Integration of mean phase difference (MPD) and phase-locking value (PLV) with time-resolved phase panels based on Hilbert and event-based phase reconstructions, enabling precise detection and visualization of synchrony regimes, including near-synchronous states (Figs. 5–11).
(ii) Quantitative demonstration that AMPARs achieve perfect synchrony (PLV = 1, MPD = 0) at substantially lower coupling than NMDARs in Mg-free conditions, and that AMPAR robustly restores tight locking under Mg block (Figs. 8–11).
(iii) Identification of a trade-off between gE_{AMPA} and gE_{NMDA} for maintaining synchrony across Mg levels, mechanistically linked to receptor kinetics and voltage dependence (Figs. 8, 10).
(iv) Systematic bifurcation analysis mapping stability across gE_{NMDA}, gE_{AMPA}, and Mg: one- and two-parameter continuations reveal LP (saddle–node of cycles), PD, and HB boundaries that align with PLV/MPD transitions and with the phase-panel summaries (μ, R) (Figs. 4A, 7A; Sections 4.1, 4.3, 4.4).

Our findings provide mechanistic support for experimental observations that AMPARs dominate rhythm generation in vivo [12, 21]. The faster kinetics of AMPAR ($\tau_{\mathrm{AMPA}} \approx 5.26$ ms versus $\tau_{\mathrm{NMDA}} \approx 151.5$ ms) in our model generate precisely timed postsynaptic potentials that enhance spike-time correlation, consistent with these experimental studies. This timing precision explains their greater efficacy in synchronizing neural activity compared to slower NMDAR-mediated signaling. In contrast, prolonged NMDAR synaptic conductance causes cumulative summation over time that blurs phase relationships, despite the longer synaptic windows. This explains why NMDARs alone achieve only near-synchrony (MPD > 0) even without magnesium block. For experimentalists, our model provides a testable framework for interpreting optogenetic studies that manipulate GluN2B/GluA1 expression, as well as pathologies that alter AMPAR/NMDAR ratios, such as schizophrenia [22].

The remainder of this paper is organized as follows. Section 2 introduces the coupled Morris–Lecar model with bidirectional AMPAR/NMDAR synapses and Mg block. Section 3 details the PLV/MPD synchronization metrics, and Section 3.3 defines the Hilbert and event-based phase reconstructions used in the phase panels and circular summaries (μ, R). Section 4 presents receptor-specific synchronization mechanisms under Mg-free and Mg-blocked conditions via bifurcation diagrams and PLV/MPD maps, with representative phase-difference panels (Figs. 6–11) that visualize the time-domain behavior behind the maps. Section 5 provides the biophysical interpretation, testable predictions, and concluding remarks.

2. Morris-Lecar model with bidirectional AMPAR-NMDAR coupling

Neural dynamics arise from the interplay of fast ion channel activity and slower biochemical processes, such as calcium and potassium fluctuations, which regulate excitability and synaptic transmission [23]. Capturing these multi-timescale interactions is crucial for accurate modeling, yet the resulting mathematical complexity often obscures the underlying mechanisms.

We examine the effects and interactions of AMPARs and NMDARs on coupled neuron dynamics using a minimal model based on two copies of the Morris-Lecar (ML) equations [24,25]. The ML model, a widely used two-dimensional system of ordinary differential equations, provides a qualitative framework for studying membrane potential oscillations. Coupled ML systems have been employed to investigate various neural behaviors, including bursting and mixed-mode oscillations [26]. Earlier respiratory-model studies revealed multiple-timescale mixed [27] and complex [28] bursting within the same Morris–Lecar framework. The well-characterized dynamics of individual ML oscillators allow for a detailed exploration of how different synaptic receptors influence coupled neuron

Table 1
The parameter values in the model defined by Eqs. (2.1) and (2.2).

Parameter values					
C_1	8 μF/cm^2	I_1	40 μA/cm^2	ϕ_1	0.01
C_2	10 μF/cm^2	I_2	60 μA/cm^2	ϕ_2	0.01
V_{Ca}	120 mV	g_{Ca}	4 mS/cm^2	K_1	−1.2 mV
V_K	−84 mV	g_K	8 mS/cm^2	K_2	18 mV
V_L	−60 mV	g_L	2 mS/cm^2	K_3	12 mV
a_{rN}	0.072 mM^{-1} ms^{-1}	a_{rA}	1.1 mM^{-1} ms^{-1}	K_4	17.4 mV
a_{dN}	0.0066 ms^{-1}	a_{dA}	0.19 ms^{-1}	K_p	5 mV
V_T	2 mV	$V_{\text{NMDA}} = V_{\text{AMPA}}$	0 mV	T_{max}	1 mM

activity. The coupled ML system is formulated as follows

$$\begin{aligned}
C_1\frac{dV_1}{dt} &= I_1 - g_{Ca}m_\infty(V_1)(V_1 - V_{Ca}) - g_K w_1(V_1 - V_K) - g_L(V_1 - V_L)\\
&\quad - gE_{\text{NMDA}}s_{21N}B(V_1)(V_1 - V_{\text{NMDA}}) - gE_{\text{AMPA}}s_{21A}(V_1 - V_{\text{AMPA}}),\\
C_2\frac{dV_2}{dt} &= I_2 - g_{Ca}m_\infty(V_2)(V_2 - V_{Ca}) - g_K w_2(V_2 - V_K) - g_L(V_2 - V_L)\\
&\quad - gE_{\text{NMDA}}s_{12N}B(V_2)(V_2 - V_{\text{NMDA}}) - gE_{\text{AMPA}}s_{12A}(V_2 - V_{\text{AMPA}}),\\
\frac{dw_1}{dt} &= \phi_1(w_\infty(V_1) - w_1)/\tau_w(V_1), \quad \frac{dw_2}{dt} = \phi_2(w_\infty(V_2) - w_2)/\tau_w(V_2),\\
\frac{ds_{21N}}{dt} &= a_{rN}T(V_2)(1 - s_{21N}) - a_{dN}s_{21N}, \quad \frac{ds_{21A}}{dt} = a_{rA}T(V_2)(1 - s_{21A}) - a_{dA}s_{21A},\\
\frac{ds_{12N}}{dt} &= a_{rN}T(V_1)(1 - s_{12N}) - a_{dN}s_{12N}, \quad \frac{ds_{12A}}{dt} = a_{rA}T(V_1)(1 - s_{12A}) - a_{dA}s_{12A},
\end{aligned} \tag{2.1}$$

with

$$\begin{aligned}
B(V_i) &= \frac{1}{1 + e^{-0.062V_i}\,[\text{Mg}^{2+}]/3.57},\\
T(V_i) &= \frac{T_{max}}{1 + e^{-(V_i - V_T)/K_p}},\\
m_\infty(V_i) &= 0.5(1 + \tanh((V_i - K_1)/K_2)),\\
w_\infty(V_i) &= 0.5(1 + \tanh((V_i - K_3)/K_4)),\\
\tau_w(V_i) &= 1\big/\cosh((V_i - K_3)/2K_4),
\end{aligned} \tag{2.2}$$

where V_i's for $i = 1, 2$ are the variables for the membrane potentials of two neurons and w_i's are gating variables for a potassium channel. The two neurons are coupled bidirectionally, through both AMPA and NMDA receptors. The gating variables $s_{ijN}(t)$ and $s_{ijA}(t)$ represent the activation dynamics of NMDA and AMPA receptors at the synapse from cell j to cell i. Moreover, the model includes key functions such as $B(V_i)$ for the voltage-dependent magnesium block of NMDAR and $T(V_i)$ for neurotransmitter release probability. Ion channel dynamics are described by $m_\infty(V_i)$, which represents the steady-state activation of calcium channels, assuming instantaneous activation and neglecting channel kinetics. Additionally, $w_\infty(V_i)$ and $\tau_w(V_i)$ govern potassium channel gating. Synaptic receptors differ fundamentally: AMPARs act rapidly and are voltage-insensitive, whereas NMDARs have slower kinetics and a voltage-dependent magnesium block $B(V_i)$ [5,14,29,30].

I_{NMDA} is modeled as $I_{\text{NMDA}} = gE_{\text{NMDA}}s_{ijN}B(V_i)(V_i - V_{\text{NMDA}})$. The gating conductance gE_{NMDA} represents the coupling strength of the NMDAR. The graph of the magnesium block $B(V_{\text{post}})$, where V_{post} is the voltage of the post-synaptic neuron, is shown in Fig. 1, where it increases with either depolarization (increased V) or lower Mg. The block can be largely removed, i.e. $B(V)$ becomes close to one, if the postsynaptic neuron is depolarized (see the black solid line at $v_1 = 25$) or when the neuron is bathed in a low magnesium medium (see the red solid line at Mg = 0). All the parameter values for the model are given in Table 1. For a detailed physiological description of the functions in Eqs. (2.1) and (2.2), readers are directed to [3,25].

In the absence of coupling (i.e., when $gE_{\text{NMDA}} = gE_{\text{AMPA}} = 0$), each ML oscillator is a two-timescale system that can be tuned to be excitable, with an attracting critical point at relatively low V, or oscillatory, with an attracting limit cycle solution. A transition between these states can be induced by increasing the parameters I_1 and I_2. However, to study synchronization, we keep I_1 and I_2 fixed at values such that in the absence of coupling, the (V_1, w_1) and (V_2, w_2) systems are both oscillatory (See Fig. 2). Then, as demonstrated in Fig. 3 (panel A), the time traces of uncoupled oscillators show asynchrony, which is reasonable as the systems are not yet coupled to affect each other. However, when the systems are coupled, as shown in Fig. 3 (panel B) for the specific coupling strengths, the coupled systems demonstrate synchrony. A primary objective of this study is to explore the conditions for oscillator synchronization and, more importantly, to examine the effects of coupling strength and Magnesium block on synchronization.

This manuscript investigates the system's dynamics across oscillatory solutions under varying coupling strengths gE_{NMDA}, gE_{AMPA}, and physiological Mg^{2+} concentrations. We emphasize critical dynamics observed at specific coupling strengths and Mg^{2+} concentrations, serving as templates for understanding patterns across other combinations of these components. The mechanisms underlying these phenomena are analyzed using two approaches in Section 3. Next, in Section 4, we examine our findings on

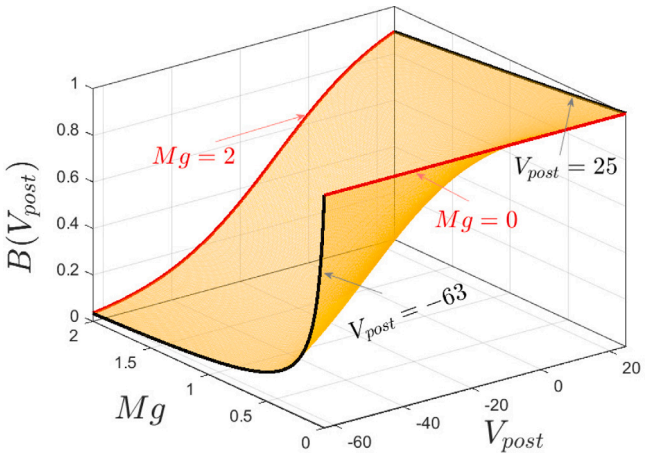

Fig. 1. Under normal physiological conditions, the NMDAR is partially blocked by magnesium ions, i.e. $B(V_{\text{post}})$ is close to zero when V_{post} is at rest and Mg ≈ 2. The block can be removed with increased V_2 or decreased Mg.

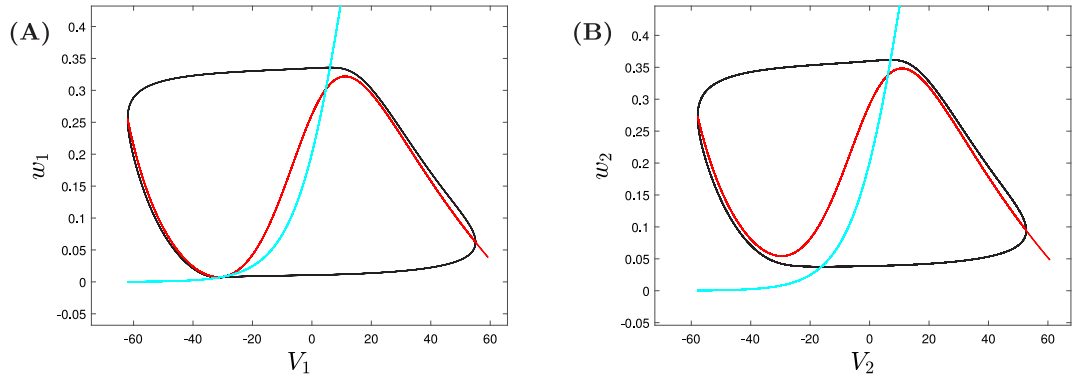

Fig. 2. Phase planes for two uncoupled ML oscillators: (A) $I_1 = 40$, (B) $I_2 = 60$. Red and cyan represent the V- and w-nullclines, respectively. Attracting periodic orbits for (V_1, w_1) and (V_2, w_2) systems are shown in black with counterclockwise flow. (For interpretation of the references to color in this figure legend, the reader is referred to the web version of this article.)

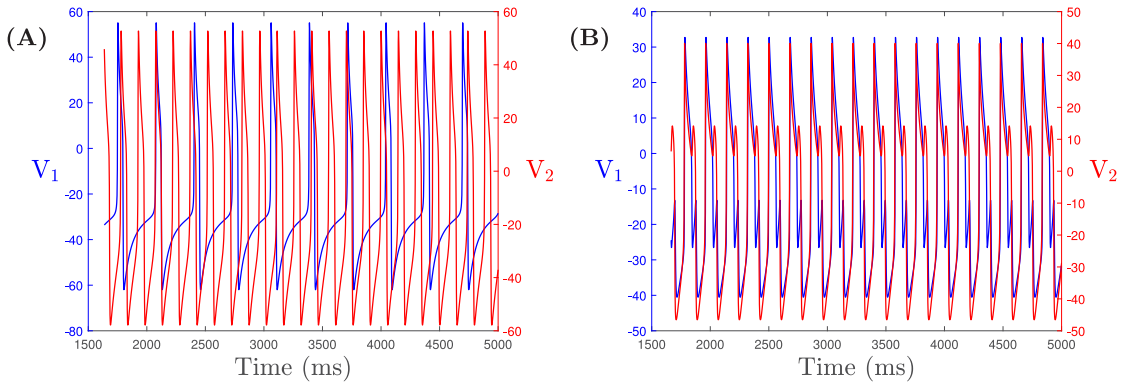

Fig. 3. Voltage traces of two Morris-Lecar oscillators. (A) Uncoupled systems ($gE_{\text{NMDA}} = gE_{\text{AMPA}} = 0$) exhibit asynchronous spiking. (B) Bidirectional coupling ($gE_{\text{NMDA}} = 1$, $gE_{\text{AMPA}} = 4$, Mg=0) induces synchrony.

the synchronization of coupled oscillators. We explore the interaction between NMDARs and AMPARs, along with the impact of magnesium block in each scenario. Furthermore, we contrast our results with experimental findings for comparison. Our results in this area may be useful for characterizing, developing models of, and analyzing experimental data models. Lastly, Section 5 is dedicated to a comprehensive discussion of our conclusions, with appendices provided at the end for reference.

To conclude this section, we highlight the need for caution when adjusting variables, as such modifications can significantly impact the accuracy and reliability of the results. For instance, setting $C_2 = 10$ and $\phi_2 = 0.01$, as shown in Table 1, results in a two-timescale system: (V_1, V_2) exhibit fast dynamics, while (w_1, w_2) evolve more slowly. However, increasing C_2 to 100 and decreasing ϕ_2 to 0.001 alters the timescale structure, causing C_2 to evolve at the same rate as w_1. This adjustment introduces a three-timescale system: V_1 remains fast, (V_2, w_1) transition to a slower timescale, and w_2 becomes super-slow. Such three-timescale structure was recently shown to support rich mixed-mode oscillations in a coupled Morris–Lecar network [26].

Remark 2.1. Baseline membrane parameters for the Morris–Lecar units are taken from standard sources [3,24]; AMPA and NMDA synaptic kinetics and voltage dependence (including Mg^{2+} block) follow widely used conductance-based formulations [5,31]. With this parameter set, each uncoupled unit lies on a tonic-spiking limit cycle born via a Hopf bifurcation (Type II excitability), consistent with the HB structure in our continuations. These choices target phase coordination rather than detailed channel biophysics, and are representative of reduced models for regular-spiking cortical or inspiratory premotor neurons.

3. Methods: Phase synchronization metrics and bifurcation analysis

Phase synchronization refers to the consistent alignment of phase angles between cyclic signals, reflecting coordinated behavior. Several metrics can assess synchronization, including coherence (capturing amplitude and phase correlations), the phase lag index (PLI) and its weighted variant (wPLI) (mitigating volume conduction artifacts) [32,33], instantaneous phase synchrony (IPS) (focusing on dynamic narrowband coupling) [34], and Granger causality in phase (evaluating directional coupling) [35]. We used the phase-locking value (PLV), a robust synchronization metric insensitive to amplitude variations, to quantify stable phase relationships between oscillators [36,37]. This makes PLV ideal for preserving phase relationships without interference from confounding factors like amplitude correlations or volume conduction.

3.1. The phase locking value approach for synchronization

Phase synchronization refers to the consistent alignment of phase angles between cyclic signals, reflecting their coordinated behavior. Among the available metrics, we employ the phase-locking value (PLV), a measure of phase synchronization between two signals defined as the magnitude of the mean phase difference, represented as a complex unit-length vector. PLV ranges from 0 (no synchronization) to 1 (perfect synchronization), with higher values indicating stronger phase consistency. It is computed as,

$$\mathrm{PLV} = \left| \frac{1}{N} \sum_{n=1}^{N} e^{i\phi_n} \right|, \tag{3.3}$$

where n indexes matched events (nearest-neighbor local minima) from the two voltage traces after discarding the initial half of events to remove transients, and N is the number of retained event pairs. Let $t_{1,n}$ and $t_{2,n}$ be the times of matched minima in V_1 and V_2, and define the signed lag $\Delta t_n = t_{1,n} - t_{2,n}$. With the local period T_n from successive minima of a reference trace (e.g., $T_n = t_{2,n+1} - t_{2,n}$), the phase difference is $\phi_n = 2\pi\,\Delta t_n / T_n \pmod{2\pi}$ to $(-\pi, \pi]$. Alternatively, instantaneous phases from Hilbert, wavelet, or Fourier methods may be sampled at these events, giving comparable results [38–40].

Conventional PLV methods sample ϕ_n at uniform time steps. We instead evaluate phases at critical points (e.g., local maxima or minima), where N is the number of detected peaks and ϕ_n their phase difference. This event-based sampling targets physiologically or dynamically significant moments, improving specificity for synchronization analysis.

3.2. Mean phase difference method for synchronization

While PLV offers reliable synchronization estimates through local maxima analysis, its effectiveness is inherently constrained by mathematical formulation and signal-dependent properties. To complement PLV, we use a mean phase difference (MPD) computed from matched extrema (local peaks/minima) of the two traces. MPD is a conventional estimator of lag synchronization (e.g., [41,42]); here it is employed alongside PLV to provide a practical, time-domain view of phase offsets.

The two measures are complementary: PLV reports the consistency of a phase relation (saturating at 1 for any stable phase-locked state), while MPD, expressed in milliseconds, distinguishes perfect synchrony from near-perfect synchrony by quantifying the residual lag. In our parameter sweeps we therefore report both, together with the phase panels in Section 4, to characterize regime boundaries consistently.

To compute MPD, we first detect local minima and maxima of the two oscillators and then calculate the distance between the closest peaks on each oscillator. This distance provides the phase-difference function, which we use to compute the MPD:

$$\mathrm{MPD} = \frac{1}{N} \sum_{n=1}^{N} |\Phi_n|, \tag{3.4}$$

where N is the number of corresponding peaks and $|\Phi_n|$ is the absolute time lag (in ms) between them. Here, Φ_n is the time offset (in ms) between the nth corresponding local peaks (or minima) of the two voltage traces. We place the absolute value inside the summation so that each term contributes the unsigned magnitude of the lag—positive whether neuron 1 leads or lags neuron 2. Averaging these unsigned lags yields the mean phase difference (MPD) in milliseconds; thus "MPD = 0 ms" coincides with perfect synchrony (PLV = 1). Larger MPD values indicate proportionally weaker phase-locking.

In the present simulations MPD ranges from 0 ms up to ∼ 70 ms, approximately one intrinsic inter-spike interval of the uncoupled Morris–Lecar neurons (∼ 65–75 ms). A lag near 70 ms therefore represents the largest possible phase offset within one cycle, indicating complete desynchronization (refer to the sidebars in Figs. 7A, 8A, and 10A). Consistent with the discussion above, MPD = 0 ms implies PLV = 1, whereas larger MPD values correspond to smaller PLV, providing an intuitive time-domain complement to the phase-locking value.

3.3. Instantaneous phase (Hilbert) and event-based phase

To visualize the phase dynamics underlying the PLV/MPD maps, we reconstruct the phase difference between the two voltage traces in two complementary ways and analyze the resulting time series $\Delta\theta(t) \in (-\pi, \pi]$. First, the instantaneous phase (Hilbert) is obtained from the analytic signal

$$z_k(t) = v_k(t) + i\,\mathcal{H}\{v_k\}(t), \qquad \theta_k(t) = \arg z_k(t), \tag{3.5}$$

where $v_k(t)$ is the membrane potential of neuron k (after detrending) and $\mathcal{H}\{\cdot\}$ denotes the Hilbert transform. The instantaneous phase difference is

$$\Delta\theta_{\mathrm{H}}(t) = \mathrm{wrap}\big(\theta_1(t) - \theta_2(t)\big) \in (-\pi, \pi]. \tag{3.6}$$

Second, an event-based phase is defined from the times of successive local minima $\{t_m^{(k)}\}_{m\geq 1}$ of $v_k(t)$. Between $t_m^{(k)}$ and $t_{m+1}^{(k)}$ the phase advances linearly by 2π,

$$\phi_k(t) = 2\pi m + 2\pi\,\frac{t - t_m^{(k)}}{t_{m+1}^{(k)} - t_m^{(k)}}, \qquad t \in [t_m^{(k)}, t_{m+1}^{(k)}), \tag{3.7}$$

and the phase difference is

$$\Delta\theta_{\mathrm{E}}(t) = \mathrm{wrap}\big(\phi_1(t) - \phi_2(t)\big) \in (-\pi, \pi]. \tag{3.8}$$

For either construction, circular summary statistics are computed over samples $\{\Delta\theta(t_j)\}_{j=1}^{J}$ taken on a uniform grid within the post-transient window:

$$\mu = \arg\left(\frac{1}{J}\sum_{j=1}^{J} e^{i\Delta\theta(t_j)}\right), \qquad R = \left|\frac{1}{J}\sum_{j=1}^{J} e^{i\Delta\theta(t_j)}\right|. \tag{3.9}$$

Here μ is the mean phase offset and $R \in [0, 1]$ measures concentration, with $R \approx 1$ indicating tight phase locking and $R \approx 0$ indicating a broad distribution. When phases are sampled uniformly in time, R is directly comparable to PLV; event-based sampling emphasizes cycle landmarks and is consistent with our MPD construction.

In all simulations the first half of each trajectory is discarded to remove transients; minima are detected with a separation constraint, and all phase differences are wrapped to $(-\pi, \pi]$. The resulting traces $\Delta\theta_{\mathrm{H}}(t)$ and $\Delta\theta_{\mathrm{E}}(t)$, together with (μ, R) and the polar histograms, corroborate the regimes identified by PLV/MPD and align with the bifurcation boundaries reported in Section 3.

3.4. Bifurcation analysis via XPP/Auto

To delineate stability regimes and critical transitions in synchronization, we employed bifurcation analysis using XPP/Auto [43]. This approach identifies key dynamical features, such as Hopf bifurcations (HB) and saddle–node bifurcations of periodic orbits (SNPO), across parameter spaces (gE_{NMDA}, gE_{AMPA}, Mg). By integrating bifurcation analysis with PLV/MPD metrics, we characterized parameter ranges for perfect and near-perfect synchrony (Figs. 4–5) and revealed bistability regions where quiescence and oscillatory states coexist (Fig. 7). The bifurcation diagrams further validated phase-locking boundaries (e.g., LP4 in Fig. 5) that were undetectable using PLV alone, highlighting the complementary strengths of these methods. The phase panels in Section 3.3 (instantaneous and event-based $\Delta\theta(t)$ with circular summaries) visually corroborate the PLV/MPD maps and sharpen the interpretation of the phase-locking boundaries revealed by XPP/Auto.

The synergy of bifurcation analysis and phase-based metrics provided a multi-scale understanding of synchronization dynamics. For instance, XPP/Auto uncovered subcritical Hopf bifurcations (Remark 4.2) and transient small-amplitude oscillations (Fig. 6), which were critical for interpreting the PLV/MPD results. This combined approach not only confirmed the robustness of synchronization regimes but also exposed parameter-dependent transitions (e.g., Mg-induced desynchronization in Fig. 9) that would remain obscured with single-method analyses [36,37]. Sections 4.1–4.4 detail these findings, demonstrating how bifurcation theory bridges phase-locking metrics with mechanistic insights into receptor-specific synchronization.

Remark 3.1. When phase differences are sampled uniformly in time, the resultant length R of the circular statistics equals the PLV; our event-based sampling yields values that closely track the PLV while emphasizing cycle landmarks.

4. Results: NMDAR and AMPAR dynamics in oscillator synchronization

Existing biological research has investigated the relationship between NMDARs and AMPARs and their impact on the synchronization of coupled oscillators [12,14,15,19,20]. However, the literature lacks conclusive mathematical evidence of a direct correlation between the slower decay of NMDARs and diminished synchronization, as compared to the effects of AMPAR activation. To further examine this potential link, we have utilized the intrinsic characteristics of these receptors to infer their roles in synchronization dynamics. Our analysis first examines synchronization induced separately by NMDARs and AMPARs, then considers their interaction effects.

4.1. Synchronization results with only NMDA receptors

The role of NMDARs in network dynamics is examined by setting gE_{AMPA} to zero. First, a magnesium-free environment is considered by setting Mg = 0 (i.e., $B(V) \equiv 1$), and the effect of the NMDAR gating conductance gE_{NMDA} is analyzed using a one-parameter bifurcation diagram (Fig. 4A). Then, a two-parameter bifurcation diagram, along with MPD and PLV metrics (Fig. 5), is used to investigate the combined influence of gE_{NMDA} and Mg on network dynamics.

Bifurcation analysis and numerical simulations (Fig. 4) reveal that NMDARs alone fail to achieve perfect synchronization (PLV = 1 and MPD = 0 ms) even when magnesium block is absent. We use the shorthand labels NPS = near-perfect synchrony (PLV = 1 with small MPD), PL = phase-locked (PLV = 1 with larger MPD), and NPL = non-phase-locked (PLV < 1). However, a near-synchronous state (NPS) with PLV = 1 and MPD $\in (5, 20)$ emerges within an intermediate range of gE_{NMDA}, bounded by two saddle–node bifurcations of periodic orbits in the full system (between LP3 at $gE_{\text{NMDA}} = 1.57$ and LP2 at $gE_{\text{NMDA}} = 4.2$, Fig. 4A).

When $gE_{\text{AMPA}} = \text{Mg} = 0$, the network system shows non-phase-locked irregular rhythms for gE_{NMDA} small (see Fig. 4B, left). As gE_{NMDA} increases to cross a saddle–node bifurcation of the periodic orbit (SNPO) (LP3 denoted by the blue square in Fig. 4A), the network dynamics transitions into a phase-locked state with a small phase difference. This nearly perfect synchrony state is denoted by the green branch in the bifurcation diagram in Fig. 4A, which initiates at the LP3 bifurcation and terminates at another SNPO bifurcation denoted as LP2 at the orange square. As a result, for $gE_{\text{NMDA}} \in (1.57, 4.2)$ between LP3 and LP2, the network exhibits a nearly perfect synchrony solution (see Fig. 4B, between LP3 and LP2).

As the value of gE_{NMDA} continues to increase beyond the LP2 bifurcation, the almost-perfect synchrony solution shifts to a different branch of phase-locked solutions which now display a larger mean phase difference (ms) (see Fig. 4B, between LP2 and LP1). Based on Fig. 4A, this new branch of phase-locked solution persists until crossing the LP1 bifurcation (marked by the black square), after which the system returns to non-phase-locked rhythms that involve low-frequency subthreshold oscillations. As gE_{NMDA} keeps increasing, the frequency of subthreshold oscillations accelerates to become as rapid as large spikes upon crossing the period-doubling (PD) bifurcation (the purple star in Fig. 4A). This PD bifurcation leads to the reappearance of phase-locked solutions with relatively large MPD values. Eventually, the phase-locked rhythms will transition into a silent (quiescent) state after crossing the Hopf bifurcation at the red circle, which occurs when gE_{NMDA} becomes large enough.

In order to explore the effects of Mg on the network dynamics, we now allow both gE_{NMDA} and Mg to vary and draw bifurcation curves in the $(\text{Mg}, gE_{\text{NMDA}})$ parameter space, as illustrated in Fig. 5. The curves of the five key bifurcations (LP3, LP2, LP1, PD and

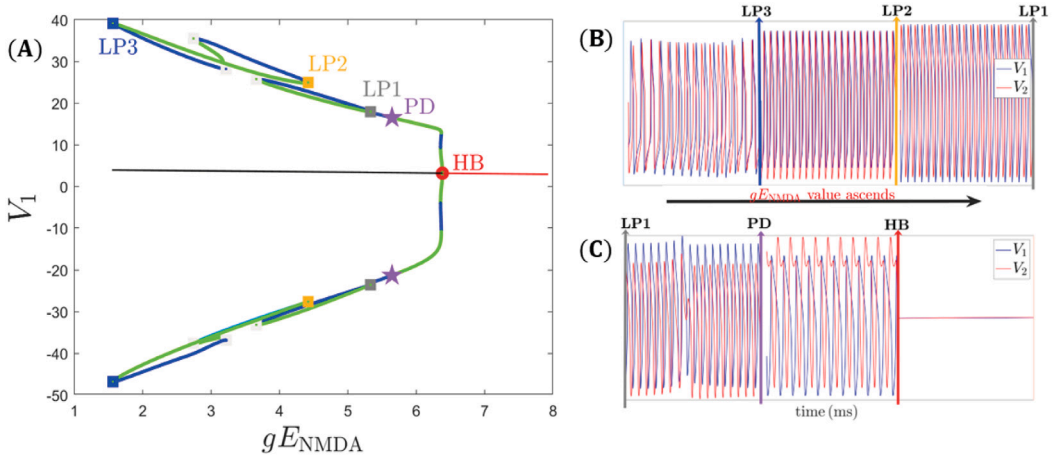

Fig. 4. Bifurcation analysis of (2.1) and representative voltage traces for various gE_{NMDA} values for $gE_{\text{AMPA}} = 0$ and Mg = 0. (A) One-parameter bifurcation diagram using XPP/Auto. The red line denotes stable fixed solutions, transitioning to instability (black line) upon crossing the Hopf bifurcation (HB) marked by a red circle. A stable periodic orbit branch (green curve) is born at the HB bifurcation and becomes unstable after the period-doubling bifurcations (PD) at the purple star. Along the periodic orbit branch, green circles represent stable oscillations, whereas blue circles indicate unstable cycles. (B,C): Voltage traces of the full system for various gE_{NMDA} values near the bifurcation points (LP3, LP2, LP1, PD and HB). (For interpretation of the references to color in this figure legend, the reader is referred to the web version of this article.)

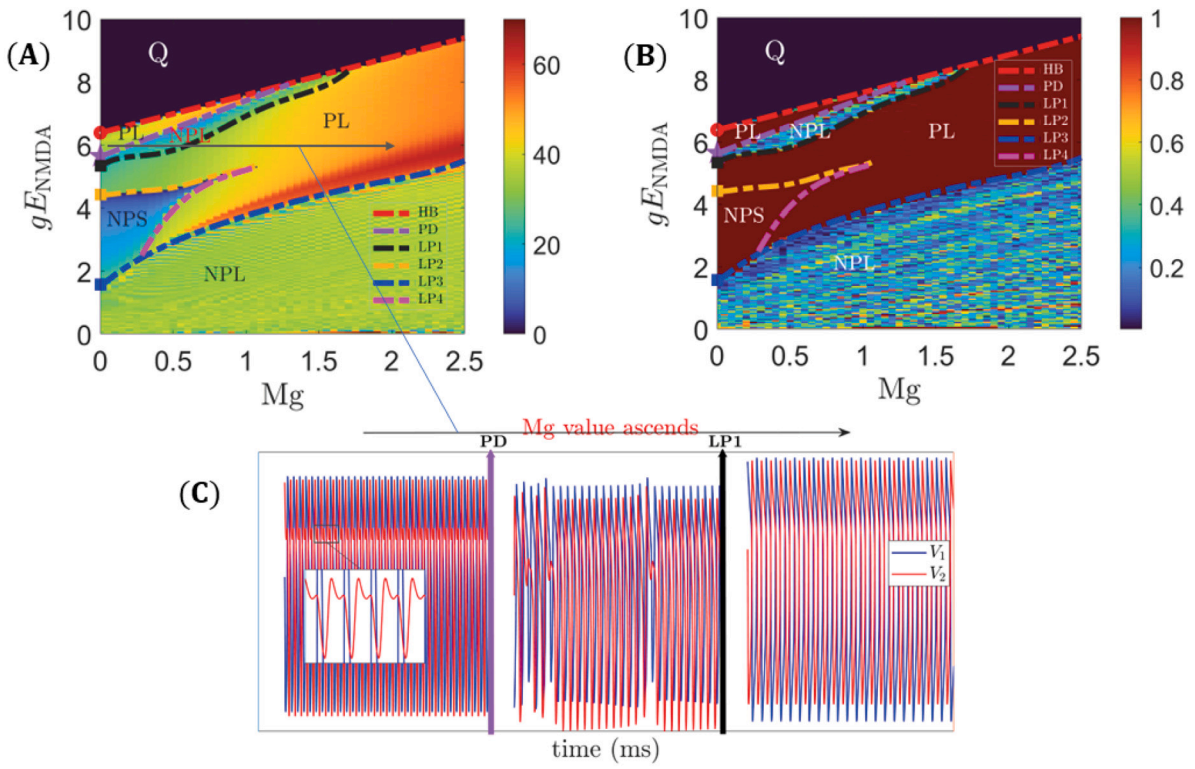

Fig. 5. The effects of gE_{NMDA} and Mg on synchronization through the mean phase difference MPD (A) and phase-locking value PLV (B) with $gE_{\mathrm{AMPA}} = 0$. The two-parameter bifurcation curves are color-coded by type: blue lines (LP3), magenta lines (LP4), orange lines (LP2), black lines (LP1), purple lines (PD), and red lines (HB), where LP stands for limit point or saddle–node bifurcation, PD stands for period-doubling bifurcation, and HB stands for Hopf bifurcation. (C) Time evolution near PD and LP1 for fixed $gE_{\mathrm{AMPA}} = 0$ and $gE_{\mathrm{NMDA}} = 6$, as the Magnesium block Mg varies from 0.1 to 0.5 to 2. Color-coded bifurcation curves (LP3: blue, LP2: orange, HB: red) demarcate regions of non-phase-locked (NPL), near-perfect synchrony (NPS), and quiescent states. (For interpretation of the references to color in this figure legend, the reader is referred to the web version of this article.)

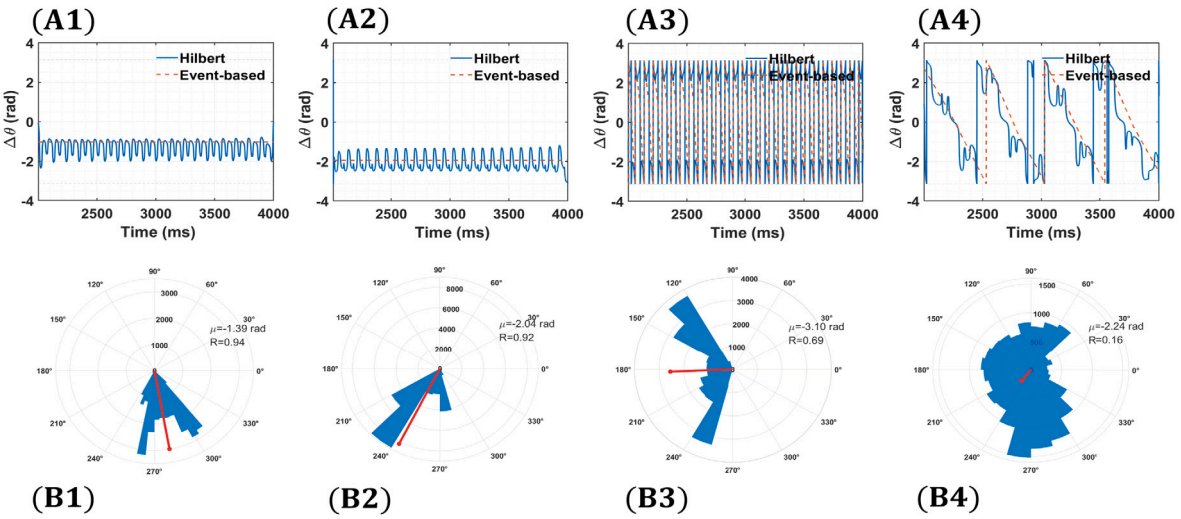

Fig. 6. Phase-difference panels for the NMDA-only slice (gE_{AMPA}=0). Columns correspond to the four parameter pairs (from left to right): (A1,B1) $(\mathrm{Mg}, gE_{\mathrm{NMDA}}) = (0, 2.5)$, (A2,B2) $(0, 5.0)$, (A3, B3) $(0, 5.8)$, (A4,B4) $(2.0, 1.0)$. Row A shows $\Delta\theta(t)$ with Hilbert (solid) and event-based (dashed) overlays; Row B shows the circular histogram of $\Delta\theta$ (Hilbert) with the red mean vector indicating (μ, R). (For interpretation of the references to color in this figure legend, the reader is referred to the web version of this article.)

HB) discussed above are color-coded consistently with the colors in Fig. 4A. These bifurcation curves coincide with the boundaries between different regions in both the MPD and PLV plots, further validating the key roles of these bifurcations in understanding the underlying mechanisms for network synchrony properties. Consistent with the one-parameter bifurcation analysis, for Mg relatively small, increasing gE_{NMDA} from zero moves the system from the non-phase-locked (NPL) region (green region in Fig. 5A and blue/green region in Fig. 5B) to the almost-perfect synchrony region (blue in Fig. 5A and red in Fig. 5B) upon crossing the LP3 bifurcation at the blue dashed line. Further increasing gE_{NMDA} shifts the system from the blue region in the MPD plot back to the green region after crossing the LP2 bifurcation. At the transition point, the MPD value experiences a sudden jump to larger values, while the PLV values remain at 1. Hence, the region above the orange line (denoted as LP2) corresponds to phase-locked solutions characterized by relatively large mean phase differences (see Fig. 5, PL region). These phase-locked solutions are lost as the continued increase of gE_{NMDA} crosses the LP1 bifurcation (the black dashed line in Fig. 5B) which initiates small-amplitude oscillations (SAOs). Phase-locked rhythms are recovered after crossing the PD bifurcation shown by the purple dashed line (see Fig. 5, PL region above the purple line). The temporary disruption of phase-locking in the NPL region through the emergence of SAOs is also illustrated in Fig. 5C. Further increasing gE_{NMDA} beyond the HB bifurcation (red dashed line) eventually suppresses all rhythms by moving the system to a quiescence region shown as black in both the MPD and PLV plots.

Fig. 5 shows that all the bifurcations curves move in the increasing gE_{NMDA} direction as Mg increases. This indicates that, to maintain a consistent level of phase locking or synchrony, the NMDA coupling strength gE_{NMDA} must increase to counteract the negative impact of the elevated Mg on the network synchrony. Moreover, a curve of SNPO branches out from the blue LP3 curve at $\mathrm{Mg} \approx 0.25$, which then meets and annihilates with the LP2 bifurcation curve at $\mathrm{Mg} \approx 1.1$. This SNPO curve is referred to as the LP4 curve, shown with magenta dashed lines in Fig. 5. It follows that the region of nearly perfect synchrony (the blue region denoted by NPS in Fig. 5A) shrinks as Mg increases. In contrast, the magnesium block has a much smaller impact on the size of the phase locking region bounded between LP3 and LP1.

Fig. 6 visualizes the phase dynamics underlying the MPD/PLV maps at four representative points along the NMDA-only slice (gE_{AMPA}=0). In (A1,B1) at $(\mathrm{Mg}, gE_{\mathrm{NMDA}})=(0, 2.5)$, $\Delta\theta(t)$ is nearly constant and its circular histogram is sharply concentrated, consistent with the near-perfect synchrony region between LP3 and LP2. In (A2,B2) at $(0, 5.0)$ the trace remains phase-locked but with a larger negative mean offset, matching the PL band above LP2. In (A3,B3) at $(0, 5.8)$, $\Delta\theta(t)$ advances rapidly across wraps and the histogram centers near π with moderate spread, illustrating large-lag phase locking near the PD/LP1 neighborhood. Finally, (A4,B4) at $(2.0, 1.0)$ a sawtooth-like drift with a broad histogram and small resultant length R reflects the loss of tight locking under magnesium block at low gE_{NMDA}. These traces and (μ, R) summaries visually corroborate the regimes and boundaries identified by MPD/PLV and the LP/HB/PD curves.

Remark 4.1. As shown in Fig. 5, bifurcation analysis of the full system enhances the insights gained from MPD and PLV methods, providing a more detailed understanding of the system's dynamics within a two-parameter framework. Notably, the MPD method can identify certain Limit Points (LP) or critical boundaries that remain undetected by the PLV method.

4.2. Synchronization results with only AMPA receptors

The role of AMPARs in network dynamics is examined by setting gE_{NMDA} to zero. Since NMDARs are absent, Mg is irrelevant in this configuration, and the analysis focuses on the AMPAR gating conductance gE_{AMPA} through a one-parameter bifurcation diagram (Fig. 7A). The $gE_{\mathrm{NMDA}} = 0$ axis in Fig. 8 further validates these results.

Bifurcation analysis and numerical simulations (Fig. 7) reveal that with only AMPARs, perfect synchronization (PLV = 1 and MPD = 0 ms) is achieved when gE_{AMPA} lies within an intermediate range ($gE_{\mathrm{AMPA}} \in (0.39, 4.0)$), bounded by two saddle–node bifurcations of periodic orbits (LP3 at $gE_{\mathrm{AMPA}} = 0.39$ and LP2 at $gE_{\mathrm{AMPA}} = 4.0$, Fig. 7A). This demonstrates AMPAR's superior efficacy in promoting synchrony compared to NMDARs, even without magnesium block.

When gE_{AMPA} is small, the network exhibits non-phase-locked irregular rhythms (Fig. 7B, left). As gE_{AMPA} increases beyond the LP3 bifurcation (blue square in Fig. 7A), the dynamics transition to a phase-locked state with negligible phase differences—the perfect synchrony state. This state, represented by the green branch in Fig. 7A, persists until the LP2 bifurcation (orange square). For $gE_{\mathrm{AMPA}} \in (0.39, 4.0)$, the network maintains perfect synchrony (Fig. 7B, middle/right), though minor phase differences may occur (e.g., at $gE_{\mathrm{AMPA}} = 0.5$).

The network does not achieve perfect synchrony for all gE_{AMPA} values between LP3 and LP2 (i.e., $gE_{\mathrm{AMPA}} \in (0.39, 4.0)$), as the mean phase difference (ms) is not always zero (e.g., at $gE_{\mathrm{AMPA}} = 0.5$). Nevertheless, these differences are negligible compared to the phase differences observed in the near-perfect synchrony state. Therefore, we classify all rhythms between LP3 and LP2 as perfect synchrony. As the value of gE_{AMPA} increases beyond the LP2 bifurcation at $gE_{\mathrm{AMPA}} = 4.0$, the perfect synchrony solution shifts to nearly perfect synchrony with PLV = 1 and MPD $\in (5, 20)$. This nearly perfect synchrony state persists until crossing another SNPO bifurcation denoted as LP5 at $gE_{\mathrm{AMPA}} = 5.34$ (see Fig. 7C, between LP2 and LP5). Upon crossing LP5, the almost-perfect synchrony solution shifts to a different branch of phase-locked solutions with a larger mean phase difference (see Fig. 7C, between LP5 and HB). Moreover, bursting dynamics begin to emerge, as depicted in the three rightmost plots between LP5 and HB in Fig. 7C. Ultimately, the phase-locked rhythms will shift into a state of quiescence upon crossing the Hopf bifurcation at the red circle ($gE_{\mathrm{AMPA}} \approx 7.335$).

Remark 4.2. As illustrated in Fig. 7A, HB is subcritical, and bistability is a common feature near such bifurcations. Therefore, the transition from oscillations to silence does not occur precisely at HB. Instead, for values of gE_{AMPA} between HB and SNPO, the system exhibits bistability, where both anti-phase-locked spiking solutions and quiescence coexist (indicated by the pink square).

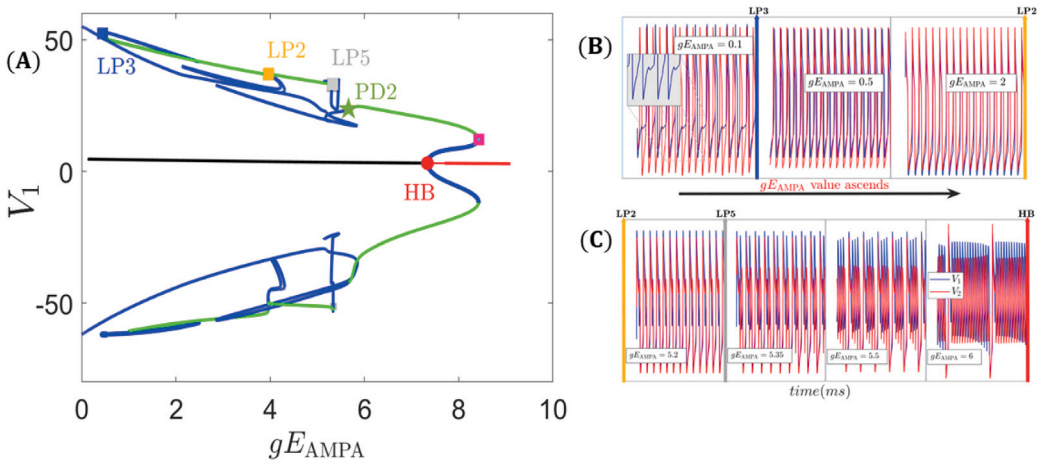

Fig. 7. Bifurcation diagram of (2.1) for fixed values of $gE_{\mathrm{NMDA}} = 0$. (A) One-parameter bifurcation diagram of the full system with respect to gE_{AMPA}, computed using XPP/Auto. (B,C): Voltage traces for various gE_{AMPA} values near the bifurcation points (LP3, LP2, LP5, PD2 and HB). As gE_{AMPA} increases from zero, the system exhibits non-phase-locked irregular network rhythms (before LP3), (nearly) perfect synchrony (between LP3 and LP2), nearly perfect synchrony (between LP2 and LP5), NPL network rhythms (between LP5 and PD2), and PL network rhythms (between PD2 and HB). In addition, small-amplitude oscillations appear as gE_{AMPA} increases across the LP2 bifurcation. The pink square denotes a new LP that other tools missed, clarifying the bistability region from HB to the LP, i.e., for $gE_{\mathrm{AMPA}} \in (7.34, 8.42)$. (For interpretation of the references to color in this figure legend, the reader is referred to the web version of this article.)

4.3. NMDAR and AMPAR interplay in the absence of magnesium

The interplay between NMDA and AMPA receptors under magnesium-free conditions (Mg = 0) is examined through two-parameter bifurcation analysis (Fig. 8). The vertical gE_{NMDA}-axis reproduces the NMDAR-only dynamics from Fig. 4, while the horizontal gE_{AMPA}-axis corresponds to the AMPAR-only results in Fig. 7.

Bifurcation analysis reveals three distinct synchronization regimes emerging under different coupling conditions. Weak coupling with $gE_{\mathrm{AMPA}} < 0.39$ and $gE_{\mathrm{NMDA}} < 1.57$ produces a non-phase-locked region visible as green and blue areas in the lower-left portion of the diagram. As coupling strengthens beyond the LP3 bifurcation marked by the blue dashed line, the system enters a perfect synchrony region shown in dark blue and red where PLV = 1 and MPD = 0. Further increases in coupling lead to near-synchrony states appearing as light blue and green regions between the LP2 (orange) and LP5 (gray) bifurcations, characterized by elevated MPD values while maintaining PLV = 1.

For small gE_{NMDA}, increasing gE_{AMPA} transitions the system from irregular rhythms to perfect synchrony (Fig. 8B). This synchrony degrades when gE_{AMPA} exceeds 4.0 (LP2), with phase differences growing discontinuously. Quiescence occurs beyond the HB bifurcation (red dashed line, $gE_{\mathrm{AMPA}} > 7.335$), consistent with the NMDAR-only case in Section 4.1.

To visualize the mechanisms behind Figs. 8, 9 shows $\Delta\theta(t)$ (Hilbert solid; event-based dashed) and the circular distribution of $\Delta\theta$ at four representative $(gE_{\mathrm{NMDA}}, gE_{\mathrm{AMPA}})$ pairs. (A1,B1) $(1.0, 0.0)$ lies below LP3 on the gE_{AMPA}=0 axis; $\Delta\theta(t)$ drifts with wraps and its histogram is broad (small R), consistent with the non-phase-locked region. (A2,B2) $(2.0, 0.0)$ falls between LP3 and LP2; $\Delta\theta(t)$ is nearly constant and the histogram is sharply concentrated with large R, matching the near-perfect synchrony band for intermediate NMDA coupling. (A3,B3) $(5.0, 1.0)$ illustrates mixed coupling above LP2: phase locking persists but with a sizable mean offset (negative μ) and moderate-large concentration, as expected for the PL band with larger lags. (A4,B4) $(0.1, 5.5)$ is AMPA-dominant; both traces align tightly and the histogram has $R \approx 1$, demonstrating robust AMPAR-driven synchrony even when NMDAR input is negligible. These panels provide time-domain confirmation of the regions and boundaries identified by the MPD/PLV maps and the LP/PD/HB curves.

The results in Fig. 8A validate and extend the NMDAR-only findings from Section 4.1, showing that while NMDAR coupling alone ($gE_{\mathrm{AMPA}} = 0$) produces near-perfect synchrony for intermediate $gE_{\mathrm{NMDA}} \in (1.57, 4.2)$ between LP3 and LP2 bifurcations, the introduction of AMPAR coupling induces qualitatively different dynamics. As gE_{AMPA} increases from zero, the system transitions from the NMDAR-mediated near-synchrony state (light blue region with PLV = 1, MPD $\in (5, 20)$) to perfect synchrony (dark blue region with PLV = 1, MPD = 0), demonstrating AMPAR's superior synchronization capability. Further increases in gE_{AMPA} drive the system through successive bifurcations: crossing LP2 (orange curve) causes an abrupt jump in MPD values while maintaining PLV = 1, LP5 (gray curve) initiates non-phase-locked dynamics, and finally the HB bifurcation (red dashed line) leads to quiescence (black region).

The AMPAR advantage is particularly evident when comparing receptor-specific effects—while NMDARs alone cannot achieve perfect synchrony, AMPARs alone establish it reliably for $gE_{\mathrm{AMPA}} \in (0.39, 4.0)$, though this effective range narrows as gE_{NMDA} increases. The phase space organization reveals complex interactions: in the green region above LP2, phase-locked solutions exhibit

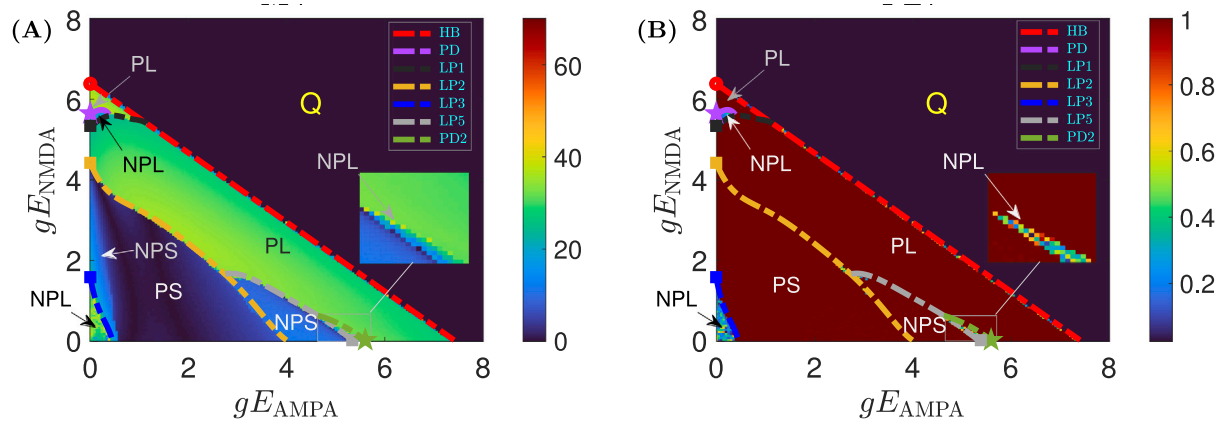

Fig. 8. Bifurcation analysis of system (2.1) with Mg = 0. (A) mean phase difference (MPD) and (B) phase-locking value (PLV) diagrams for gE_{NMDA}-gE_{AMPA} parameter space. Limit points (LP, squares) occur at $gE_{\mathrm{AMPA}} = 0.39, 4.00, 5.34$ when $gE_{\mathrm{NMDA}} = 0$, with period-doubling (PD, pentagram) at 5.6 and Hopf bifurcation (HB, circle) at 7.335.

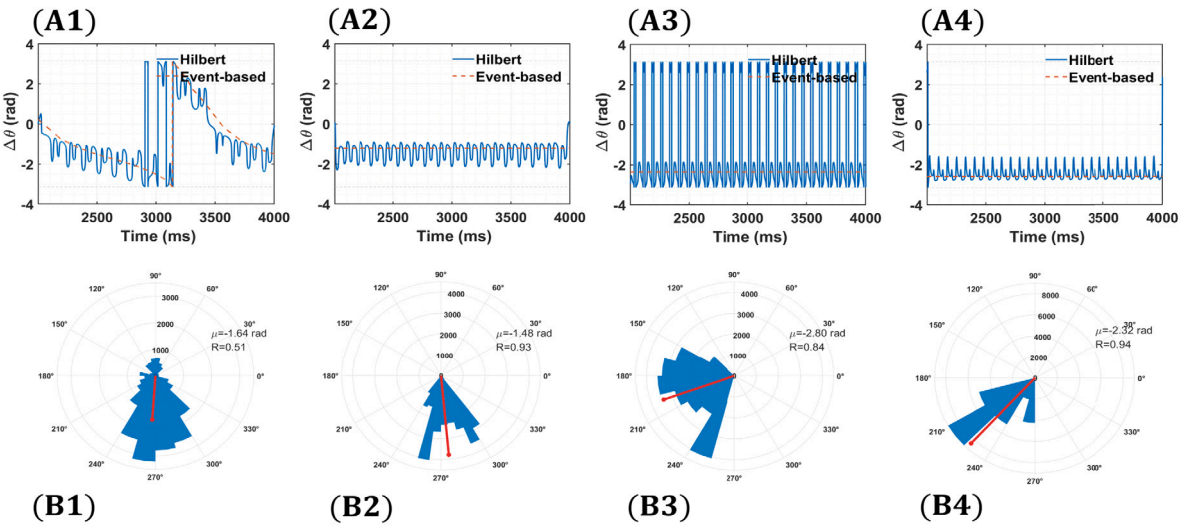

Fig. 9. Phase-difference panels at fixed Mg = 0. Columns correspond to the four $(gE_{\mathrm{NMDA}}, gE_{\mathrm{AMPA}})$ pairs (left→right): (A1,B1) $(1.0, 0.0)$, (A2,B2) $(2.0, 0.0)$, (A3,B3) $(5.0, 1.0)$, (A4,B4) $(0.1, 5.5)$. Row A: $\Delta\theta(t)$ (Hilbert solid; event-based dashed). Row B: polar histogram of $\Delta\theta$ (Hilbert) with red mean vector (μ, R). (For interpretation of the references to color in this figure legend, the reader is referred to the web version of this article.)

larger mean phase differences, while for minimal gE_{AMPA}, increasing gE_{NMDA} past LP2 transforms near-synchrony into phase-locked states with growing phase differences (Fig. 4B). Subsequent bifurcations introduce richer dynamics—LP1 (black square) triggers low-frequency subthreshold oscillations, the PD bifurcation (purple star) restores large spiking activity, and ultimately strong coupling induces quiescence through the HB bifurcation. These results collectively demonstrate how the competing timescales of NMDAR and AMPAR kinetics shape the parameter space for network synchronization.

4.4. Synchronization dynamics in the presence of Mg

This section examines the interactions between AMPAR and NMDAR under magnesium block conditions to further elucidate their functional roles. Since the one-parameter bifurcation analysis with respect to gE_{AMPA} closely resembles the Mg-free case (Fig. 7), we instead focus on the effects of magnesium block, emphasizing its influence on NMDAR and AMPAR dynamics.

When only NMDAR is active and AMPAR is absent, the system fails to reach full synchrony in the presence of magnesium block, as seen near the vertical line in Fig. 10(A). Furthermore, Fig. 10(B) shows that this region does not exhibit phase-locking until gE_{NMDA} exceeds a threshold ($gE_{\mathrm{NMDA}} > 5$). However, introducing even a small gE_{AMPA} initially drives the system toward near-perfect synchrony. As gE_{AMPA} increases, the system progressively attains perfect synchrony, represented by the blue region

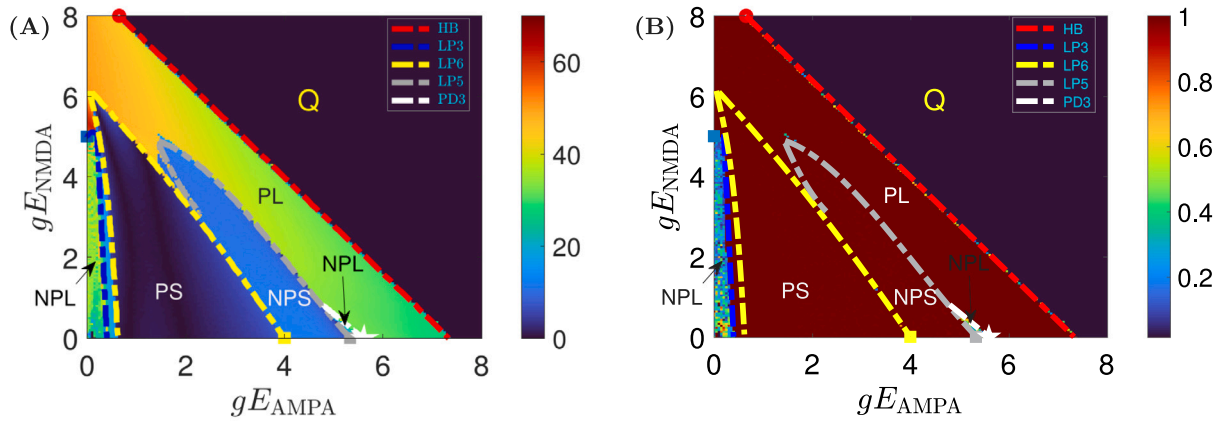

Fig. 10. In the presence of Magnesium block, i.e., when Mg = 2. MPD (panel A) and PLV (panel B) for the bifurcation diagrams with respect to gE_{NMDA} and gE_{AMPA}. The squares, and circles mark limit points (LP), and Hopf bifurcations (HB), respectively. For $gE_{\mathrm{NMDA}} = 0$, LP occurs at $gE_{\mathrm{AMPA}} = 0.389, 4$, and 5.336, and HB occurs at $gE_{\mathrm{AMPA}} = 7.335$.

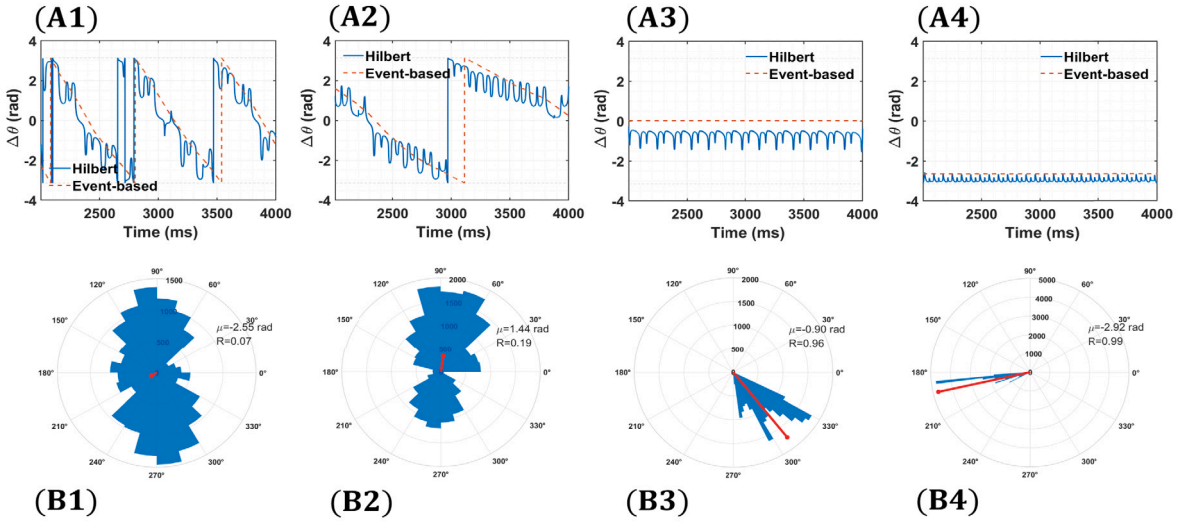

Fig. 11. Phase-difference panels at fixed Mg = 2 (strong Mg block on NMDA). Columns correspond to the four $(gE_{\mathrm{NMDA}}, gE_{\mathrm{AMPA}})$ pairs (left→right): (A1,B1) (2.0, 0.0), (A2,B2) (4.0, 0.0), (A3,B3) (1.0, 1.0), (A4,B4) (1.0, 5.0). Row A: $\Delta\theta(t)$ (Hilbert solid; event-based dashed). Row B: polar histogram of $\Delta\theta$ (Hilbert) with red mean vector (μ, R).

in Fig. 10(A). Notably, in the two-parameter bifurcation diagram (Fig. 10), the intersection of the blue bifurcation curve with the vertical gE_{NMDA}-axis corresponds to the LP3 blue lines in Fig. 5.

A comparison between Figs. 8(A) and 10(A) reveals that without magnesium block, NMDAR alone can sustain near-perfect synchrony without AMPAR involvement. In contrast, magnesium block disrupts this synchrony, underscoring the critical interplay between NMDAR and magnesium in shaping synchronization dynamics.

In the absence of AMPAR, Fig. 5(A) demonstrates a significant decline in synchronized activity, nearing complete desynchronization. NMDAR, however, helps maintain partial synchrony, particularly in regions where magnesium block effects are weak or absent (see the light blue region in Fig. 5).

Specifically, when magnesium block is absent (Mg = 0), the system achieves nearly perfect synchrony without AMPAR for $1.57 \leq gE_{\mathrm{NMDA}} \leq 4.42$ (Figs. 5(A) and 8(A)). In contrast, with magnesium present (Mg $\neq$ 0), synchrony is unattainable regardless of gE_{NMDA} (Fig. 10).

To complement Figs. 10, 11 shows $\Delta\theta(t)$ (Hilbert solid; event-based dashed) and the circular distribution of $\Delta\theta$ at four $(gE_{\mathrm{NMDA}}, gE_{\mathrm{AMPA}})$ pairs under strong Mg^{2+} block. (A1,B1) (2.0, 0.0) (NMDA-only) exhibits drifting $\Delta\theta(t)$ with wraps and a broad histogram (small R), consistent with the non-phase-locked region at low gE_{NMDA}. (A2,B2) (4.0, 0.0) remains Mg-limited: $\Delta\theta(t)$ shows slow drift or intermittent plateaus and a moderately broad histogram (intermediate R), illustrating near-boundary/partial locking.

(A3,B3) $(1.0, 1.0)$ (balanced, small) produces weak phase locking: $\Delta\theta(t)$ meanders around a mean with a moderately concentrated histogram (mid-range R). (A4,B4) $(1.0, 5.0)$ (AMPA-dominant) attains robust locking despite Mg block: $\Delta\theta(t)$ is nearly constant with a narrow histogram and large R, demonstrating AMPA-driven restoration of tight phase concentration. These panels provide time-domain confirmation of the regimes and boundaries identified by the MPD/PLV maps and the LP/HB structure in Fig. 10.

4.5. Analyzing perfect synchrony: AMPAR's success, NMDAR's challenges

Within this subset, we explore an analysis of the underlying factors influencing the achievement of perfect synchronization in coupled oscillators with only AMPARs within a specific range of gE_{AMPA}. Conversely, we investigate the reasons behind the inability to attain perfect synchronization with only NMDAR, even when the magnesium block is absent (refer to the region near the vertical line in Fig. 8).

Examining the first two equations of the coupled ML system (2.1), it becomes evident that gE_{AMPA} and gE_{NMDA} play pivotal roles in influencing the behavior of V_1 and V_2 through the open fractions of AMPA and NMDA, namely $s_{ijA}(t)$ and $s_{ijN}(t)$. Focusing on V_1 exclusively (disregarding V_2), we analyze the behaviors of s_{21A} and s_{21N} and their impacts on the dynamics of (V_1, V_2).

The distinct decay kinetics of AMPA and NMDA receptor-mediated synaptic conductances are characterized in response to a single presynaptic spike. The decay time constants were derived from biophysical parameters, where the AMPA receptor decay rate $a_{dA} = 0.19\,\text{ms}^{-1}$ yields $\tau_{\text{AMPA}} = 1/a_{dA} \approx 5.26\,\text{ms}$, consistent with experimental observations of fast AMPA receptor deactivation. In contrast, the NMDA receptor decay rate $a_{dN} = 0.0066\,\text{ms}^{-1}$ results in $\tau_{\text{NMDA}} = 1/a_{dN} \approx 151.51\,\text{ms}$, reflecting prolonged current due to slow glutamate unbinding and voltage-dependent Mg^{2+} block kinetics. The presynaptic action potential (spike) at 50 ms triggers neurotransmitter release modeled by a sigmoidal function $T(V_{\text{pre}})$, while the conductance decay was fitted post-spike to exclude the rising phase. Notably, the AMPA conductance rapidly returns to baseline within approximately 30 ms, enabling precise transient signaling, whereas the NMDAR synaptic conductance persists beyond 500 ms, facilitating time-dependent summation and synaptic plasticity. The 29.1-fold slower decay of NMDA receptors aligns with established AMPA/NMDA ratios in synaptic transmission, underscoring their complementary roles in neural computation (see Fig. 12).

Removing the magnesium block restores synchrony for certain positive values of gE_{NMDA} when AMPARs are absent, as illustrated in Fig. 5 (A) and the left panel in Fig. 8(A) for $3 < gE_{\text{NMDA}} \leq 4.1$. This finding aligns with [12], which shows that NMDAR alone can generate and sustain synchrony without magnesium blocks in solution.

In the presence of the magnesium block, perfect synchrony occurs when $gE_{\text{AMPA}} \geq 0.5$ (refer to Fig. 10). However, in the absence of AMPARs ($gE_{\text{AMPA}} = 0$), the system fails to synchronize regardless of the gE_{NMDA} value. This observation reinforces the assertion that AMPARs play a superior role compared to NMDAR in synchronization.

Removing NMDA does not affect synchronized activity other than increasing burst amplitude. However, synchronized activity is almost disrupted when removing AMPA. Fig. 8 shows that NMDAR can compensate for the lack of AMPARs and keep some regions partially synchronized when there are no magnesium blocks. However, when magnesium blocks are present, the system loses synchrony without AMPARs. This agrees with the results of [12].

NMDARs and AMPARs show an inverse correlation regarding achieving perfect synchronization in coupled oscillators. As shown in Fig. 8, when the NMDA (resp. AMPA) coupling strength increases, there is a need to decrease the AMPA (resp. NMDA) coupling strength to maintain perfect synchronization. This opposite relationship is worsened in the presence of magnesium block (see Fig. 10) and remains consistent across different contexts. For example, increasing the NMDA (or AMPA) coupling strength requires reducing the AMPA (or NMDA) coupling strength to keep oscillations going and prevent a transition to the quiescence region. This connection is illustrated by the red line showing the Hopf bifurcations in Figs. 8 and 10.

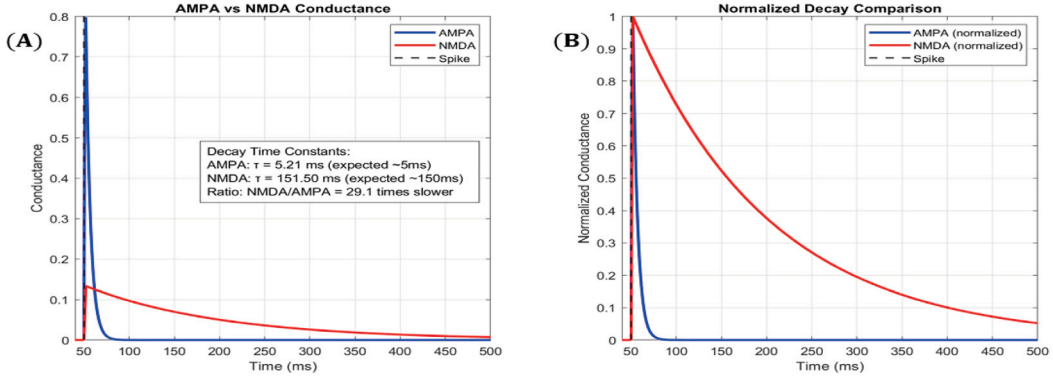

Fig. 12. Conductance dynamics of AMPA and NMDA receptors after a presynaptic spike. (**A**) Raw synaptic conductances showing fast AMPA decay ($\tau = 5.21\,\text{ms}$) and slow NMDA decay ($\tau = 151.50\,\text{ms}$). (**B**) Normalized conductances highlighting NMDA's 29.1-fold slower decay. The vertical dashed line marks the spike time at 50 ms.

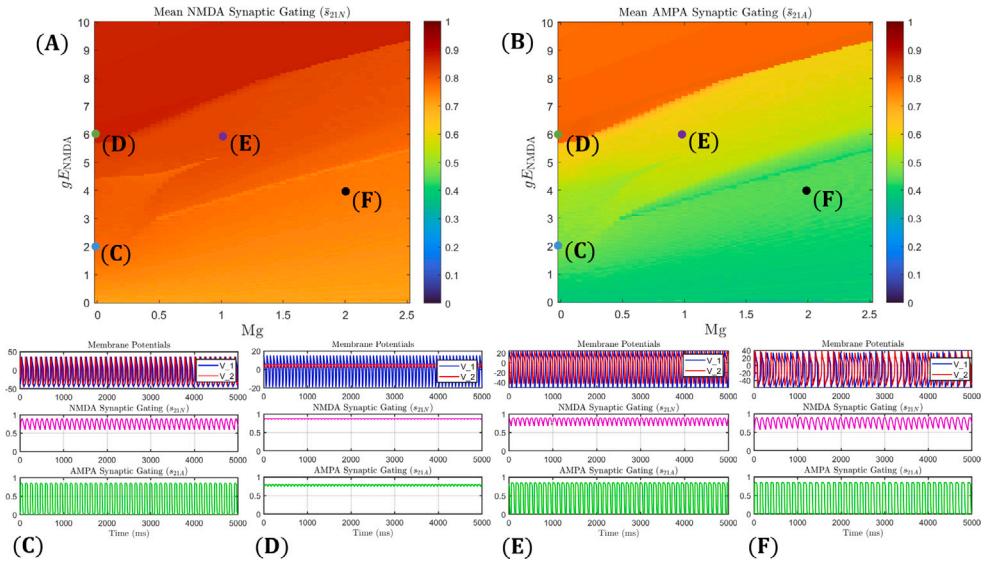

Fig. 13. Steady-state synaptic gating with $g_{E\mathrm{AMPA}} = 0$. (A–B) Pseudocolor maps of mean open fractions $\bar{s}_{21N}$ (NMDA) and $\bar{s}_{21A}$ (AMPA) over Mg^{2+} and $g_{E\mathrm{NMDA}}$. (C–D) Horizontal line-cuts from (A–B) at fixed $g_{E\mathrm{NMDA}}$: $\bar{s}_{21N}$ remains near-saturated over wide Mg^{2+} ranges, while $\bar{s}_{21A}$ stays modest due to fast decay. (E–F) Vertical line-cuts from (A–B) at fixed Mg^{2+}, showing dependence on $g_{E\mathrm{NMDA}}$ (e.g., Mg ≈ 0 vs. physiological Mg ≈ 2 mM). Color bars denote normalized open-channel fractions (0: closed, 1: fully open).

Fig. 13 presents Pseudocolor plots of steady-state mean synaptic gating variables, $\bar{s}_{21N}$ (NMDA) and $\bar{s}_{21A}$ (AMPA), plotted against extracellular magnesium concentration (Mg^{2+}) and NMDAR coupling strength (gE_{NMDA}). AMPA coupling is set to zero ($gE_{\mathrm{AMPA}} = 0$), allowing for an isolated examination of NMDA dynamics. The colorbars indicate the average fraction of open synaptic channels, with values normalized between 0 (fully closed) and 1 (fully open). These visualizations provide insight into how synaptic gating changes under different physiological conditions.

The results highlight the well-known magnesium-dependent behavior of NMDAR. When magnesium levels are low (Mg ≈ 0), $\bar{s}_{21N}$ remains close to 1 across all values of gE_{NMDA}, indicating minimal voltage-dependent blockade and strong NMDA activation. However, as magnesium concentration increases (Mg > 1), NMDA activity becomes significantly suppressed, even at higher NMDA coupling strengths. This effect is a direct consequence of the voltage-dependent Mg-block, which restricts NMDAR activation unless the membrane is sufficiently depolarized to dislodge magnesium from the channel.

AMPAR activity follows a different pattern. Despite the absence of direct AMPA coupling ($gE_{\mathrm{AMPA}} = 0$), $\bar{s}_{21A}$ exhibits a modest level of activation, with mean values between approximately 0.2 and 0.4. This activation is primarily driven by presynaptic voltage fluctuations (V_2), which influence neurotransmitter release through $T(V_2)$. Additionally, AMPARs have much faster decay kinetics ($a_{dA} = 0.19\,\mathrm{ms}^{-1}$) compared to NMDAR ($a_{dN} = 0.0066\,\mathrm{ms}^{-1}$), resulting in a lower steady-state $\bar{s}_{21A}$. These differences in receptor kinetics further emphasize the distinct roles of NMDARs and AMPARs in synaptic transmission.

Despite the prolonged activation of NMDAR conductance, NMDAR is less effective than AMPAR in supporting synchrony due to its slow decay kinetics and voltage-dependent Mg-block. Table 1 shows that NMDAR has a much slower decay rate ($a_{dN} = 0.0066\,\mathrm{ms}^{-1}$) than AMPAR ($a_{dA} = 0.19\,\mathrm{ms}^{-1}$), leading to extended activation. While this prolonged activity supports synchrony over longer timescales, it delays synaptic transmission, making NMDAR less effective for high-frequency synchrony, which requires rapid and precise timing. Additionally, NMDAR activity is suppressed at higher extracellular magnesium concentrations (Mg^{2+}) due to its voltage-dependent Mg-block, limiting its role in synchrony unless the membrane is sufficiently depolarized. In contrast, AMPAR, with its fast decay and lack of Mg-block, enables rapid and precise synaptic communication, making it more effective for synchrony, particularly at higher frequencies. Thus, despite its prolonged activation, NMDAR's slow kinetics and Mg-block make it less suitable for synchrony than AMPAR.

4.6. Neuronal synchronization in heterogeneous networks

To evaluate whether the synchronization mechanisms observed in pairwise-coupled oscillators generalize to larger networks, we analyzed a heterogeneous network of 30 Morris-Lecar neurons with distributed parameters. This investigation aimed to determine if AMPARs retain their synchronization advantage over NMDARs in complex, heterogeneous systems and how magnesium block influences collective dynamics.

The synchrony score χ, computed across the network, reveals consistent trends with earlier results. For Mg = 2 (Fig. 14A), robust synchronization ($\chi \approx 1$) occurs at intermediate gE_{AMPA} values, mirroring the perfect synchrony regime in the two-neuron model. Introducing NMDAR coupling ($gE_{\mathrm{NMDA}} > 0$) marginally improves synchrony but requires significantly higher coupling strengths

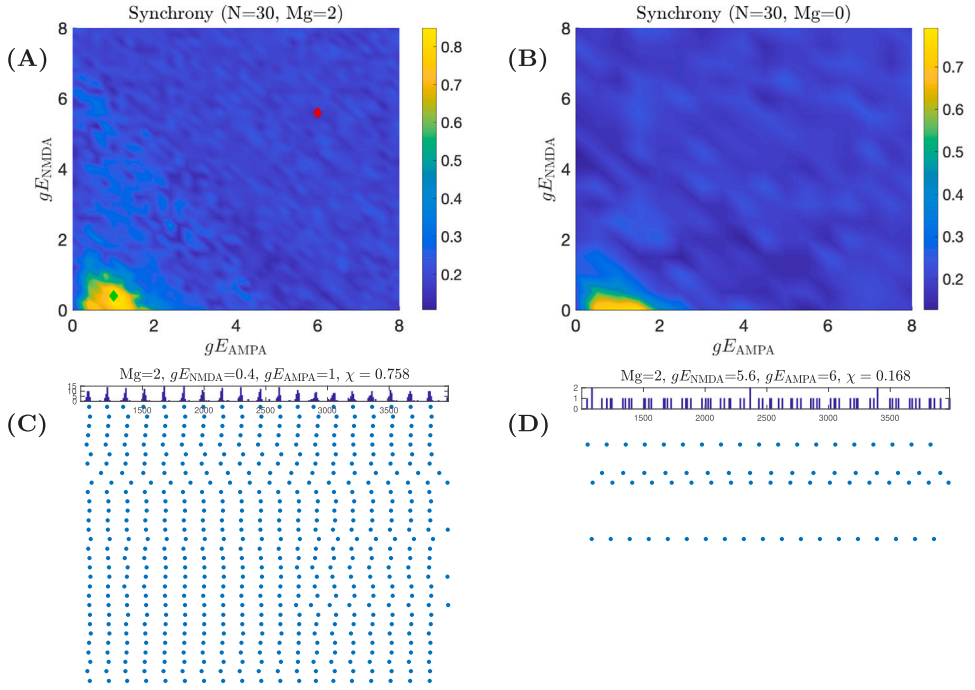

Fig. 14. Synchrony score χ of a 30-node network with heterogeneous ML equations, plotted vs. the AMPAR gating conductance gE_{AMPA} and NMDAR gating conductance gE_{NMDA}, for (A) Mg = 2 and (B) Mg = 0. (C, D) The spike raster of individual neuron activity with parameters given by the green and red diamonds in panel (A). (For interpretation of the references to color in this figure legend, the reader is referred to the web version of this article.)

to compensate for magnesium block, aligning with the inverse AMPAR-NMDAR relationship identified in Section 4.5. Spike raster plots (Figs. 14C–D) confirm that high gE_{AMPA} induces coherent firing, whereas reliance on NMDARs alone results in dispersed spiking. Without magnesium block (Mg = 0, Fig. 14B), NMDARs sustain partial synchrony at elevated coupling strengths, though less effectively than AMPARs. These results validate that AMPAR synchronization scales to larger networks, while NMDAR efficacy remains constrained by slow kinetics and magnesium block, even in heterogeneous configurations.

5. Discussion and conclusion

This study provides a comprehensive computational analysis of the differential roles of AMPA and NMDA receptors in neural synchronization using coupled Morris–Lecar oscillators. Our findings highlight AMPAR's crucial role in precise spike-time synchronization due to its fast kinetics, whereas slow NMDAR dynamics inherently limit synchronization efficacy despite prolonged activation.

The phase panels (Figs. 6, 9, 11) visualize the time-domain mechanisms that underlie the PLV/MPD regimes and two-parameter bifurcation structure. In tightly locked regions, $\Delta\theta(t)$ is nearly constant and the circular histograms are sharply concentrated (large R); near phase-detuning boundaries, $\Delta\theta(t)$ exhibits slow drifts or intermittent plateaus with moderate concentration; under strong Mg^{2+} block or weak coupling, $\Delta\theta(t)$ ramps with wraps and the histograms are broad (small R). These signatures agree with the LP/PD/HB boundaries identified in Section 4.

While our focus on two excitatory cells isolates the specific role of NMDA-mediated coupling, many brain rhythms emerge from the interplay between excitation and inhibition. Intrinsic currents can be equally influential; pharmacologically blocking the persistent sodium current reshapes respiratory rhythm generation, illustrating how non-synaptic conductances modulate network output [44]. In larger circuits, slow NMDA currents are often linked to reverberatory activity or bistability rather than fast synchronous oscillations [45–47]. Including inhibitory neurons and heterogeneous cell types is therefore a natural extension that could reveal how NMDA conductances shape rhythmogenesis in more realistic networks (see the consolidated *Future directions* below).

Qualitatively, AMPA antagonists are expected to disrupt population rhythms, whereas NMDA currents can sustain slower, less precise activity in low-Mg conditions; the panels in Figs. 6 and 9 reflect these trends. Three testable predictions follow from our diagrams: (i) relieving Mg^{2+} block (e.g., via depolarization) or modestly increasing gE_{AMPA} should move networks from near-synchrony (moderate R, MPD > 0) to tight locking (large R, MPD ≈ 0) at fixed gE_{NMDA}; (ii) increasing Mg^{2+} at fixed couplings

should broaden the $\Delta\theta$ distribution and reduce R; (iii) co-tuning $(gE_{\mathrm{AMPA}}, gE_{\mathrm{NMDA}})$ along the perfect-synchrony manifolds inferred from our two-parameter maps should preserve high PLV and small MPD despite parameter drift.

The key findings reveal that the rapid decay kinetics of AMPARs ($\tau_{\mathrm{AMPA}} \approx 5.26\,\mathrm{ms}$) facilitate precise timing coordination of neural activity through transient, sharply timed postsynaptic potentials. In contrast, NMDARs exhibit significantly slower decay kinetics ($\tau_{\mathrm{NMDA}} \approx 151.51\,\mathrm{ms}$) that result in prolonged synaptic conductance, which ultimately degrade phase relationships and synchronization fidelity. Quantitative analysis demonstrates that AMPARs achieve perfect synchronization (PLV = 1, MPD = 0) at substantially lower coupling strengths ($gE_{\mathrm{AMPA}} \in (0.39, 4.0)$) compared to NMDARs, which can only reach near-synchrony (MPD > 0) even with increased coupling strength. These timing effects are visible in the phase panels (Figs. 6, 9, 11) as narrow circular histograms with large R and nearly constant $\Delta\theta(t)$ under AMPA-dominated conditions.

Our results further show that the voltage-dependent magnesium block of NMDARs imposes additional constraints on synchronization, requiring at least 2.5 times stronger coupling to overcome its suppressive effects. These findings are consistent across different network configurations, as validated by both pairwise-coupled oscillators and heterogeneous 30-neuron networks. The MPD-PLV metric developed in this study provides enhanced detection of near-synchronous states that conventional methods often miss, offering a more complete understanding of neural coordination dynamics. Future work could merge this metric with recent linear-response and variational phase-analysis frameworks for limit cycles with hard boundaries [48,49], yielding a complementary, model-agnostic view of how receptor kinetics tune phase resetting and entrainment.

Beyond timing mechanisms, effective synaptic drive depends on ionic composition and channel microphysics. Poisson–Nernst–Planck (PNP) analyses predict how unequal diffusion coefficients, permanent charge, finite-ion-size effects, and flux-ratio structure shift apparent reversal potentials and driving forces [50–55]. Such shifts would be expected to nudge the PLV/MPD boundaries we map here, especially under changes to extracellular composition (e.g., Mg^{2+}) or fixed charge near synaptic sites.

Future directions. Several promising directions emerge from this research. First, incorporating calcium dynamics and synaptic plasticity will allow us to probe how Ca^{2+}-dependent rules shape phase coordination under AMPA/NMDA coactivation at realistic extracellular calcium levels and timing windows [56]. Second, extending the model with richer, experimentally grounded receptor kinetics (e.g., state-dependent AMPAR conformational control and pH/temperature-sensitive recovery from desensitization; spatial alignment of asynchronous release with NMDAR nanocolumns) could clarify how microphysiology gates network-scale synchrony [57,58]. Third, we will incorporate hybrid coupling architectures that combine chemical synapses with electrical (gap-junction) connectivity; recent work indicates that electrical synapses coordinate interneuron responses to shared chemical inputs and reconfigure mesoscale dynamics, suggesting a principled route to robust synchronization across heterogeneity [59–61]. Fourth, *ion-transport-aware conductances*: couple synaptic/reversal parameters to PNP-style submodels so that diffusion asymmetries, permanent charge, steric effects, and flux-ratio constraints co-determine V_{rev} and synaptic drive in situ [50–55]. This would test how ionic microphysics moves bifurcation curves (LP/HB/PD) and reshapes perfect- vs. near-synchrony domains. Finally, at the mesoscopic level, next-generation mean-field formulations with explicit nonlinear, voltage-dependent NMDAR Mg^{2+} block provide a practical bridge between detailed conductance models and large-scale network predictions, and can be layered onto our present framework [62].

CRediT authorship contribution statement

Hamid Mofidi: Writing – review & editing, Writing – original draft, Visualization, Validation, Conceptualization. **Yangyang Wang:** Writing – original draft, Methodology, Conceptualization.

Data and code availability

Parameter sweeps and scripts (XPP/AUTO continuation files and PLV/MPD/phase-panel analysis code) are available from the authors upon reasonable request.

Declaration of competing interest

The authors declare that there are no conflicts of interest or competing interests related to this work. We affirm that our professional judgment concerning the validity of this research has not been influenced by any secondary interests, such as financial gain or personal relationships.

Acknowledgments

HM acknowledges partial funding from the National Natural Science Foundation of China (grant 1241101557). This work was supported in part by NIH/NIDA R01DA057767 to YW, as part of the CRCNS program.

Data availability

Parameter sweeps and scripts (XPP/AUTO continuation files and PLV/MPD/phase-panel analysis code) are available from the authors upon reasonable request.

References

[1] Doelling KB, Assaneo MF. Neural oscillations are a start toward understanding brain activity rather than the end. PLoS Biol 2021;19(5):e3001234.
[2] Varela F, Lachaux J, Rodriguez E. The brainweb: phase synchronization and large-scale integration. Nature Rev Neurosci 2001;4:229–39.
[3] Ermentrout B, Terman D. Mathematical foundations of neuroscience. Springer; 2010.
[4] Traynelis SF, Wollmuth LP, McBain CJ, et al. Glutamate receptor ion channels: structure, regulation, and function. Pharmacol Rev 2010;62(3):405–96.
[5] Jahr CE, Stevens CF. A quantitative description of NMDA receptor-channel kinetic behavior. J Neurosci 1990;10:1830–7.
[6] Butera RJ, Rinzel J, Smith JC. Models of respiratory rhythm generation in the pre-Bötzinger complex. I. Bursting pacemaker neurons. J Neurophysiol 1999;82(1):382–97.
[7] Toporikova N, Butera R. Two types of independent bursting mechanisms in inspiratory neurons: An integrative model. J Comput Neurosci 2011;30(3):515–28.
[8] Wang Y, Rubin JE. Timescales and mechanisms of sigh-like bursting and spiking in models of rhythmic respiratory neurons. J Math Neurosci 2017;7:1–39.
[9] Park C, Rubin JE. Cooperation of intrinsic bursting and calcium oscillations underlying activity patterns of model pre Bötzinger complex neurons. J Comput Neurosci 2013;34:345–66.
[10] Funk GD, Smith JC, Feldman JL. Generation and transmission of respiratory oscillations in medullary slices: role of excitatory amino acids. J Neurophysiol 1993;70:1497–515.
[11] Greer JJ, Smith JC, Feldman JL. Role of excitatory amino acids in the generation and transmission of respiratory drive in neonatal rat. J Physiol 1991;437:727–49.
[12] Morgado-Valle C, Feldman JL. NMDA receptors in pre Bötzinger complex neurons can drive respiratory rhythm independent of AMPA receptors. J Physiol 2007;582:359–68.
[13] Poon CS, Zhou Z, Champagnat J. NMDA receptor activity in utero averts respiratory depression and anomalous long-term depression in newborn mice. J Neurosci 2000;20:RC73.
[14] Castellani GC, Quinlan EM, Cooper LN, Shouval HZ. A biophysical model of bidirectional synaptic plasticity: dependence on AMPA and NMDA receptors. Proc Natl Acad Sci USA 2001;98:12772–7.
[15] Gauck V, Jaeger D. The contribution of NMDA and AMPA conductances to the control of spiking in neurons of the deep cerebellar nuclei. J Neurosci 2003;23:8109–18.
[16] Tikidji-Hamburyan RA, Govindaiah G, Guido W, Colonnese MT. Synaptic and circuit mechanisms prevent detrimentally precise correlation in the developing mammalian visual system. eLife 2023;12:e84333.
[17] Crowe DA, Willow A, Blackman RK, DeNicola AL, Chafee MV, Amirikian B. A prefrontal network model operating near steady and oscillatory states links spike desynchronization and synaptic deficits in schizophrenia. eLife 2024;13:e79352.
[18] Susin E, Destexhe A. A network model of the modulation of γ oscillations by NMDA receptors in cerebral cortex. ENeuro 2023;10(11). ENEURO.0157–23.2023.
[19] Huang S, Chen L, Bladen C, Stys PK, Zamponi GW. Differential modulation of NMDA and AMPA receptors by cellular prion protein and copper ions. Mol Brain 2018;11:62.
[20] Micheli P, Ribeiro R, Giorgetti A. A mechanistic model of NMDA and AMPA receptor-mediated synaptic transmission in individual hippocampal CA3-CA1 synapses: A computational multiscale approach. Int J Mol Sci 2021;22:1536.
[21] Funk GD, Johnson SM, Smith JC, Dong XW, Lai J, Feldman JL. Functional respiratory rhythm generating networks in neonatal mice lacking NMDAR1 gene. J Neurophysiol 1997;78:1414–20.
[22] Uhlhaas PJ, Linden DE, Singer W, Haenschel C, Lindner M, Maurer K, et al. Dysfunctional long-range coordination of neural activity during gestalt perception in schizophrenia. J Neurosci 2006;26:8168–75.
[23] Borges FS, Protachevicz PR, Souza DLM, Bittencourt CF, Gabrick EC, Bentivoglio LE, et al. The roles of potassium and calcium currents in the bistable firing transition. Brain Sci 2023;13:1347.
[24] Morris C, Lecar H. Voltage oscillations in the barnacle giant muscle fiber. Biophys J 1981;35(1):193–213.
[25] Nan P, Wang Y, Kirk V, Rubin JE. Understanding and distinguishing three-time-scales oscillations: A case study in a coupled Morris-Lecar system. SIAM J Appl Dyn Syst 2015;14:1518–57.
[26] N.A. Phan, Wang Y. Mixed-mode oscillations in a three-timescale coupled Morris–Lecar system. Chaos: An Interdiscip J Nonlinear Sci 2024;34.
[27] Wang Y, Rubin JE. Multiple timescale mixed bursting dynamics in a respiratory neuron model. J Comput Neurosci 2016;41:245–68.
[28] Wang Y, Rubin JE. Complex bursting dynamics in an embryonic respiratory neuron model. Chaos: An Interdiscip J Nonlinear Sci 2020;30:043127.
[29] Destexhe A, Mainen ZF, Sejnowski TJ. Synthesis of models for excitable membranes, synaptic transmission and neuromodulation using a common kinetic formalism. J Comput Neurosci 1994;1:195–230.
[30] Li C, Gulledge AT. Nmda receptors enhance the fidelity of synaptic integration. ENeuro 2021;8:1–19.
[31] Destexhe A, Mainen ZF, Sejnowski TJ. Kinetic models of synaptic transmission. Methods Neuronal Model 1998;1–26.
[32] Stam CJ, Nolte G. Phase lag index: Assessment of functional connectivity from multi channel EEG and MEG with diminished bias from common sources. Hum Brain Mapp 2009;28:1178–93.
[33] Vinck A, Oostenveld R, van Wingerden M, Battaglia F. An improved index of phase-synchronization for electrophysiological data in the presence of volume-conduction, noise and sample-size bias. NeuroImage 2011;55:1548–65.
[34] Paluš M, Vejmelka M. Directionality of coupling from bivariate time series: How to avoid false causalities. Phys Rev E 2003;77:026214.
[35] Barnett L, Barrett AB, Seth AK. Granger causality and transfer entropy are equivalent for Gaussian variables. Phys Rev Lett 2008;103:238701.
[36] Tass P, Rosenblum MG, Weule J, Kurths J, Pikovsky A, Volkmann J, et al. Detection of n:m phase locking from noisy data: application to magnetoencephalography. Phys Rev Lett 1998;81(15):3291–4.
[37] Ahn S, Rubchinsky LL. Short desynchronization episodes prevail in synchronous dynamics of human brain rhythms. Chaos 2013;23:013138.
[38] Aydore S, Pantazis D, Leahy RM. A note on the phase locking value and its properties. NeuroImage 2013;74:231–44.
[39] Celka P. Statistical analysis of the phase-locking value. IEEE Signal Process Lett 2007;14:577–80.
[40] Lachaux J-P, et al. Measuring phase synchrony in brain signals. Hum Brain Mapp 2014;8(4):194–208.
[41] Boccaletti S, Valladares DL. Characterization of intermittent lag synchronization. Phys Rev E 2000;62(6):7497–500.
[42] Pikovsky A, Rosenblum M, Kurths J. Synchronization: A universal concept in nonlinear sciences. Cambridge University Press; 2001.
[43] Ermentrout Bard. Simulating, analyzing, and animating dynamical systems: A Guide to XPPAUT for researchers and students. Society for Industrial and Applied Mathematics (SIAM); 2002.
[44] Phillips RS, Rubin JE. Effects of persistent sodium current blockade in respiratory circuits depend on the pharmacological mechanism of action and network dynamics. PLoS Comput Biol 2019;15:e1006938.
[45] Wang Xiao-Jing, Buzsáki György. Gamma oscillation by synaptic inhibition in a hippocampal interneuronal network model. J Neurosci 1996;16:6402–13.
[46] Kopell Nancy, Ermentrout Bard. Rhythms and synchrony in a cortical network model. Proc Natl Acad Sci USA 2004;101:15482–7.
[47] Destexhe Alain. Network reverberation, fluctuations and infinite variance in cortical circuits with NMDA conductances. Nature Neurosci 2000;3:934–40.

[48] Wang Y, Gill JP, Chiel HJ, Thomas PJ. Shape versus timing: linear responses of a limit cycle with hard boundaries under instantaneous and static perturbation. SIAM J Appl Dyn Syst 2021;20:701–44.
[49] Wang Y, Gill JP, Chiel HJ, Thomas PJ. Variational and phase response analysis for limit cycles with hard boundaries, with applications to neuromechanical control problems. Biol Cybernet 2022;116:687–710.
[50] Mofidi H, Liu W. Reversal potential and reversal permanent charge with unequal diffusion coefficients via classical Poisson–Nernst–Planck models. SIAM J Appl Math 2020;80:1908–35.
[51] Mofidi H, Eisenberg B, Liu W. Effects of diffusion coefficients and permanent charge on reversal potentials in ionic channels. Entropy 2020;22(325):1–23.
[52] Mofidi H. Reversal permanent charge and concentrations in ionic flows via Poisson-Nernst-Planck models. Quart Appl Math 2021;79:581–600.
[53] Fu Y, Liu W, Mofidi H, Zhang M. Finite ion size effects on ionic flows via Poisson-Nernst-Planck systems: Higher order contributions. J Dynam Differential Equations 2022;1–25.
[54] Mofidi H. New insights into the effects of small permanent charge on ionic flows: A higher order analysis. Math Biosci Eng 2024;21(5):6042–76.
[55] Mofidi H, Hadadifard F, Zhang M. Analysis of flux-ratio bifurcation in ionic flows via classical Poisson–Nernst–Planck models. Stud Appl Math 2025;155(2):e70087.
[56] Inglebert Y, Aljadeff K, Franks NP, van Rossum MCW, Fellin T, Delescluse J, et al. Synaptic plasticity rules with physiological calcium levels. ELife 2020;9:e55744.
[57] Ivica J, Graus S, Viswanathan V, Korkut E, Bartol TF, Shraiman BS, et al. Proton-triggered rearrangement of the AMPA receptor N-terminal domain shapes receptor kinetics and synaptic transmission. Nat Struct Mol Biology 2024;31:1124–34.
[58] Li S, Li Y, Chan KMH, Shawn CM, Ho CC, Tian L, et al. Asynchronous release sites align with NMDA receptors in hippocampal synapses. Nat Commun 2021;12:677.
[59] Choi U, Kim H, Park S, Hwang M, Park H, Kim R, et al. Presynaptic coupling by electrical synapses coordinates a cerebellar inhibitory network. Proc Natl Acad Sci 2021;118(19):e2022599118.
[60] Gutiérrez GJ, Roxin AS. Gap junctions: the missing piece of the connectome. Curr Biology 2023;33(24):R1369–87.
[61] Martin EA, Tenorio AE, Pereda AE. Understanding the molecular and cell biological mechanisms of electrical synapse formation and function. Annu Rev Physiol 2020;82:219–41.
[62] Sheheitli H, Destexhe A. Incorporating slow NMDA-type receptors with nonlinear voltage-dependent magnesium block in a next-generation neural mass model: derivation and dynamics. J Comput Neurosci 2024;52:73–98.